



## OpenAIR@RGU

### The Open Access Institutional Repository at Robert Gordon University

<http://openair.rgu.ac.uk>

This is an author produced version of a paper published in

Journal of Thermal Spray Technology (ISSN 1059-9630, eISSN 1544-1016)

This version may not include final proof corrections and does not include published layout or pagination.

#### Citation Details

##### Citation for the version of the work held in 'OpenAIR@RGU':

FAISAL, N.H., AHMED, R., KATIKANENI, S.P., SOUENTIE, S. and GOOSEN, M.F.A., 2016. Development of plasma-sprayed molybdenum carbide-based anode layers with various metal oxides for SOFC. Available from *OpenAIR@RGU*. [online]. Available from: <http://openair.rgu.ac.uk>

##### Citation for the publisher's version:

FAISAL, N.H., AHMED, R., KATIKANENI, S.P., SOUENTIE, S. and GOOSEN, M.F.A., 2016. Development of plasma-sprayed molybdenum carbide-based anode layers with various metal oxides for SOFC. *Journal of Thermal Spray Technology*, Vol 24(8), pp. 1415-1428.

#### Copyright

Items in 'OpenAIR@RGU', Robert Gordon University Open Access Institutional Repository, are protected by copyright and intellectual property law. If you believe that any material held in 'OpenAIR@RGU' infringes copyright, please contact [openair-help@rgu.ac.uk](mailto:openair-help@rgu.ac.uk) with details. The item will be removed from the repository while the claim is investigated.

The final publication is available at Springer via <http://dx.doi.org/10.1007/s11666-015-0315-2>.

# Development of plasma sprayed molybdenum carbide-based anode layers with various metal oxides for SOFC

N. H. Faisal<sup>1,2\*</sup>, R. Ahmed<sup>3,2</sup>, S. P. Katikaneni<sup>4</sup>, S. Souentie<sup>4</sup>, M. F. A. Goosen<sup>5</sup>

<sup>1</sup> School of Engineering, Robert Gordon University, Garthdee Road, Aberdeen, AB10 7GJ, UK

<sup>2</sup> College of Engineering, Alfaisal University, P.O. Box 50927, Riyadh 11533, Saudi Arabia

<sup>3</sup> School of Engineering and Physical Sciences, Heriot-Watt University, Edinburgh, EH14 4AS, UK

<sup>4</sup> Research & Development Center, Saudi Aramco, Dhahran 31311, Saudi Arabia

<sup>5</sup> Office of Research & Graduate Studies, Alfaisal University, P.O. Box 50927, Riyadh 11533, Saudi Arabia

## Abstract

Air plasma sprayed (APS) coatings provide an ability to deposit a range of novel fuel cell materials at competitive costs. This work develops three separate types of composite anodes (Mo-Mo<sub>2</sub>C/Al<sub>2</sub>O<sub>3</sub>, Mo-Mo<sub>2</sub>C/ZrO<sub>2</sub>, Mo-Mo<sub>2</sub>C/TiO<sub>2</sub>) using a combination of APS process parameters on Hastelloy<sup>®</sup>X for application in intermediate temperature proton conducting solid oxide fuel cells. Commercially available carbide of molybdenum powder catalyst (Mo-Mo<sub>2</sub>C) and three metal oxides (Al<sub>2</sub>O<sub>3</sub>, ZrO<sub>2</sub>, TiO<sub>2</sub>) were used to prepare three separate composite feedstock powders to fabricate three different anodes. Each of the modified composition anode feedstock powders included a stoichiometric weight ratio of 0.8:0.2. The coatings were characterized by scanning electron microscopy, energy dispersive spectroscopy, X-ray diffraction, nanoindentation and conductivity. We report herein that three optimized anode layers of thicknesses between 200 to 300 μm and porosity as high as 20% for Mo-Mo<sub>2</sub>C/Al<sub>2</sub>O<sub>3</sub> (250 μm thick) and Mo-Mo<sub>2</sub>C/TiO<sub>2</sub> (300 μm thick) and 17% for Mo-Mo<sub>2</sub>C/ZrO<sub>2</sub> (220 μm thick), controllable by a selection of the APS process parameters with no addition of sacrificial pore-forming material. The nanohardness results indicate the upper

layers of the coatings have higher values than the subsurface layers in coatings with some effect of the deposition on the substrate. Mo-Mo<sub>2</sub>C/ZrO<sub>2</sub> shows high electrical conductivity.

*Keywords:* air plasma spray (APS), molybdenum carbide, anode, SOFC.

*\*Corresponding author - Email: [n.h.faisal@rgu.ac.uk](mailto:n.h.faisal@rgu.ac.uk); Tel: +44-1224 262438*

## 1. Introduction

The development of low-cost fuel cell materials with high durability and lower operating temperatures is the key technical challenge facing solid oxide fuel cell (SOFC) technology in auxiliary power units (e.g. transportation). The future of SOFC technology depends upon the development of new materials (electrode, electrolyte, interconnects) which can be used to manufacture SOFC's in a cost effective manner. Development of SOFC materials present a number of technological challenges. Low mechanical strength, slow start-up time (i.e. in minutes), and serious anode deterioration represent some of these technological challenges. The high operating temperatures (600-1000 °C) place additional durability requirements on SOFCs materials [1-4]. The development of low-cost materials with high durability at lower operating temperatures is the key technical challenge facing SOFC technology. Reducing the operating temperature to intermediate range can lower the cost but also reduce the reaction rate [3]. Some of the recent articles [4-8] summarize most of the known SOFC materials (electrodes, electrolytes, interconnects) and their manufacturing alternatives, relevant to modern requirements. However, the scope of this work is to present a development of air plasma sprayed (APS) new anode materials for SOFC systems. **Figure 1** summarizes SOFC components and arrangement. In SOFC, the fuel is fed to the anode (negative electrode) and air (oxidant) is fed to the cathode (positive electrode). Electrochemical oxidation and reduction reactions take place at the electrodes to produce

electric current. In the traditional SOFC, oxygen (from air) is reduced by a porous cathode producing oxide ions (-ve) which migrate through a solid electrolyte to the porous anode and react with the fuel (e.g. n-dodecane, dry He, H<sub>2</sub> or CH<sub>4</sub>) forming H<sub>2</sub>O and/or CO<sub>2</sub>. The electrolyte may conduct either oxygen (SOFC) or hydrogen ions (PC-SOFC). In a PC-SOFC, the reaction product (water vapor) is evolved at the cathode side instead of at the anode (fuel side) as is the case for oxygen ion-conducting SOFC.

Traditional wet ceramic techniques based on tape casting, screen printing, and co-sintering of layers are the state-of-the-art processing methods for the fabrication of SOFC single cells, and therefore widely adopted and intensively investigated [2, 5]. However, these techniques face several problems [5-6], which include: (a) use of multiple separate instruments, (b) increased capital cost due to high temperature firing, thermal expansion mismatch strain and cracking during high-temperature firing steps, and (c) inter-reaction between adjacent cell layers at high-temperature firing steps and d) limitation of high-temperature sintering of anode and metallic interconnect materials. Heo *et al.* [9-10] recently developed a new efficient type of fuel cell that runs directly on hydrocarbons. They developed a proton-conducting solid oxide fuel cell (PC-SOFC) with strong anodes made from a casted pellets of composite Mo<sub>2</sub>C-ZrO<sub>2</sub>/C materials. The developed cell showed efficient oxidation of hydrocarbons (in the presence of water) including methane, ethane, propane and butane at temperatures between 100 to 300 °C. This operating temperature was much lower than currently used (600 to 1000 °C). Moreover, the Mo<sub>2</sub>C-ZrO<sub>2</sub>/C fuel cell was cleaner, emitting nothing apart from carbon dioxide. It performed best with the heavier molecules of butane gas, which is easiest to store for transport purposes. The operation of the fuel cell at 300 °C can reduce the start-up time as well as prevent carbon deposition on the anode surface.

The Mo<sub>2</sub>C can be used in anodes for hydrocarbon oxidation, because it shows high tolerance towards sulfidation as well as carbon deposition. However, the power densities

obtained by Heo *et al.* [9-10] were substantially lower (in 10's of  $\text{mW}/\text{cm}^2$ ) than those reported for other SOFCs (in 100's of  $\text{mW}/\text{cm}^2$  [5-6]). This was attributed to large thickness ( $\sim 1000 \mu\text{m}$ ) of the electrolyte (i.e.  $\text{Sn}_{0.9}\text{In}_{0.1}\text{P}_2\text{O}_7$ ) produced by the casting method. This work concluded a need to manufacture thinner electrolyte films casted on Platinum/C cathode. In a related investigation by Brungs *et al.* [11], the effect of the support on the stability of the  $\text{Mo}_2\text{C}$  catalyst (prepared by temperature programmed reaction, TPRE method) was investigated using ethane. It was demonstrated that at elevated pressure, the choice of the support for the  $\text{Mo}_2\text{C}$  dry reforming catalyst is crucial to catalyst stability, and the order of catalyst stability was found to be in this order ( $\text{Mo}_2\text{C}-\text{Al}_2\text{O}_3 > \text{Mo}_2\text{C}-\text{ZrO}_2 > \text{Mo}_2\text{C}-\text{SiO}_2 > \text{Mo}_2\text{C}-\text{TiO}_2$ ).  $\text{Mo}_2\text{C}$  also is an excellent dehydrogenation catalyst [12] with activity comparable to that of Pt [13]. Considering these key factors, composite powder materials ( $\text{Mo}_2\text{C}-\text{ZrO}_2$ ) can potentially be used for an improved anode performance in direct hydrocarbon SOFCs.

Efforts have also been made to increase anode thickness (around 1000-2000  $\mu\text{m}$ ) to support the electrolyte layer and providing the mechanical strength to the cell, particularly for auxiliary power units. However, the increased thickness of anode leads to a reduction of gas permeability. It also results in a slow flux of fuel to the anode/electrolyte interface and of the produced  $\text{H}_2\text{O}$  away from this interface. As a consequence, there is an excessive change in fuel composition, i.e.,  $\text{H}_2:\text{H}_2\text{O}$  ratio, resulting in an equivalent increase of the oxygen potential and therefore a decrease in the voltage of the cell for a given current density.

In the case of a thin anode, the fuel and also the produced  $\text{H}_2\text{O}$  can be easily transported. Pore structure and permeability factor are very important for the efficient operation of the anode and the whole of SOFC. For that reason, the characterization of the microstructure and its parameters, e.g. total porosity, open porosity, and pore size distribution can be used as control parameters for the development of anode material. Existing

methodology of casting anodes for SOFC technology is inadequate for manufacturing thinner anodes for improved efficiency. This work therefore targets thermal spray technique (e.g. air plasma spray, APS) to fabricate SOFC anode layer using composite powder materials (Mo-Mo<sub>2</sub>C/Al<sub>2</sub>O<sub>3</sub>, Mo-Mo<sub>2</sub>C/ZrO<sub>2</sub>, Mo-Mo<sub>2</sub>C/TiO<sub>2</sub>).

## 2. Materials and Methods

### 2.1 Material Selection and Properties

The Hastelloy®X material was chosen as a disc substrate (interconnect in SOFC). The disc substrates (20 mm diameter and 4.76 mm thick) were supplied by Haynes International Limited, Manchester, UK. This material is a nickel-chromium-iron-molybdenum alloy that possesses an exceptional combination of oxidation resistance, fabricability and high-temperature strength. The material elemental composition (wt.%) included Cr: 21.73, Fe: 19.34, Mo: 8.44, C: 0.075, Co: 1.20, Mn: 0.67, W: 0.54, Si: 0.34, Cu: 0.17, Al: 0.09, P: 0.012, Ti: 0.01, B: 0.002, S: 0.002, Ni: balance. It has also been found to be exceptionally resistant to stress-corrosion cracking in petrochemical applications. An ideal interconnect serves to keep oxidant and fuel gases separate from one another. It should also have high electronic conductivity, excellent impermeability, and chemical stability under both oxidizing and reducing conditions.

The molybdenum (Mo, a transition metal) has a high melting point, high thermal conductivity, high electrical conductivity, low thermal expansion coefficient, and good high temperature creep properties. As a metallic matrix with carbide, the Mo with Mo<sub>2</sub>C (i.e. Mo-Mo<sub>2</sub>C) feedstock powder material (**Fig. 2a**) was an agglomerated and sintered spheroidal powder designed for coating application using atmospheric plasma spray (APS). This powder material (Metco 64) was supplied by Sulzer Metco, Germany. It produces coatings that are harder and more resistant to abrasion while maintaining many of the useful properties of pure

molybdenum coatings, such as high scuff resistance, low frictional characteristics and high toughness. The powder material elemental composition included 97.3% Mo, 2.1% C, 0.1% O and 1% others, whereas, the nominal particle size distribution was  $-90+38\ \mu\text{m}$ . The Mo-Mo<sub>2</sub>C powder melting point was 2620 °C.

The white alumina (Al<sub>2</sub>O<sub>3</sub>) feedstock powder material was available in a wide variety of shapes (fused and crushed) and sizes with angular and blocky morphology. Alumina is a hard, wear resistant material that is chemically inert and stable at high temperatures. In addition, the high purity grades exhibit excellent electrical insulation (dielectric characteristics) and thermal conductivity. The addition of Al<sub>2</sub>O<sub>3</sub> can improve electrical properties by grain boundary modification [14]. This powder material (METCO-105SFP) was supplied by Sulzer Metco, Germany. The powder material elemental composition included Al<sub>2</sub>O<sub>3</sub> (99.5 wt.%), Fe<sub>2</sub>O<sub>3</sub> (0.03 wt.%), Na<sub>2</sub>O (0.15 wt.%), SiO<sub>2</sub> (0.01 wt.%) and CaO (0.01 wt.%), whereas, the normal particle size distribution was  $-31+3.9\ \mu\text{m}$ . The Al<sub>2</sub>O<sub>3</sub> powder melting point was 2054 °C.

The Zirconia (ZrO<sub>2</sub>) feedstock powder material was available in a wide variety of shapes and sizes (fused and crushed). Zirconia is stable in oxidizing and mildly reducing atmospheres. It reacts with carbon, nitrogen and hydrogen at temperatures above 2200 °C. It is inert to acids and bases at room temperature with the exception of HF and does not react with the refractory metals up to 1400 °C. This powder material (40453) was supplied by Alfa Aesar, UK which consists of Zirconium(IV) oxide, calcia stabilized, 99.4% (metals basis excluding Hf). Stabilized zirconia is used in oxygen sensors and fuel cell membranes because it has the ability to allow oxygen ions to move freely through the crystal structure at high temperatures. For calcia stabilized zirconia, the electrical (ionic) conductivity can be 0.0237 S.cm<sup>-1</sup> (800 °C), 0.1109 S.cm<sup>-1</sup> (1000 °C), 0.3212 S.cm<sup>-1</sup> (1200 °C), and makes it one of the most useful electro-ceramics [15]. The powder material elemental composition included 96%

ZrO<sub>2</sub> and 4% CaO, whereas, the normal particle size distribution was -100+325 μm. The ZrO<sub>2</sub> powder melting point was 2700 °C.

The dark grey to black titanium oxide (TiO<sub>2</sub>) feedstock powder material was available in a wide variety of shapes (fused, crushed, agglomerated and sintered) and sizes with angular, blocky or spheroidal morphology. Titanium oxides are used for a wide variety of applications that include wear resistant coatings and electrically conductive coatings. This agglomerated/sintered and spheroidal powder material (METCO-6231A) was supplied by Sulzer Metco, Germany. The addition of TiO<sub>2</sub> can improve electrical properties by grain boundary modification. This powder can be designed to produce coatings with low electrical resistivities and potentially superior tribological properties. The powder material elemental composition included TiO<sub>2</sub> (balance wt.%), Al<sub>2</sub>O<sub>3</sub> (<0.1 wt.%), Fe<sub>2</sub>O<sub>3</sub> (<0.1 wt.%), SiO<sub>2</sub> (<0.1 wt.%) and all others (<0.5 wt.%), whereas, the normal particle size distribution was -105+32 μm. The TiO<sub>2</sub> powder melting point was 1843 °C.

## *2.2 Air Plasma Spraying of SOFC Anode Coatings*

The carbide of molybdenum powder catalyst (Mo-Mo<sub>2</sub>C) and three metal oxides (e.g., Al<sub>2</sub>O<sub>3</sub>, ZrO<sub>2</sub>, TiO<sub>2</sub>, all beneficial for catalyst stability) were used to prepare three composite feedstock powders (Mo-Mo<sub>2</sub>C/Al<sub>2</sub>O<sub>3</sub>, Mo-Mo<sub>2</sub>C/ZrO<sub>2</sub>, Mo-Mo<sub>2</sub>C/TiO<sub>2</sub>) to fabricate three different anodes. Each of the modified composition anode feedstock powders included a stoichiometric weight ratio of 0.8:0.2. The substrate (Hastelloy®X) was grit blasted using 100 μm to 250 μm size quartz particles. Coating process parameters which have greater influence on coating thickness, coating hardness, porosity level of coating withstanding capability were identified (e.g. from various published literatures [e.g. 5, 8] and know-how). Various experiments were conducted to determine working range of above factors. Various controllable parameters namely angle, current, hydrogen flow, spray distance and feed rate

were identified and air plasma spraying was carried out by varying the parameters as prescribed by the design matrix (mainly varying the spray distance such as 75 mm, 100 mm and 200 mm and feed rate such as 35 g.min<sup>-1</sup>, 70 g.min<sup>-1</sup> and 100 g.min<sup>-1</sup>) and coatings were produced over Hastelloy®X substrate.

Plasma spray deposition was carried out at an industrial facility (Monitor Coating Limited, UK), using an APS system (Metco 3MB gun and the nozzle used is a 3M7A-GP, Metco). As shown in **Fig. 2b,c**, the disc specimens were mounted on assembly in circular holes which were cut on steel plate and then mounted on jaw chuck in coating chamber. The powders were directly sprayed on to the grit blasted substrate and bond coat was not used. Different combinations of APS process parameters were used to carry out the trial runs. To fix the limits of the considered factors, a key criteria that the anode layer must have high porosity were adopted. The difference in melting temperatures of main feed-stock powder Mo-Mo<sub>2</sub>C (2620 °C) and metal oxides [Al<sub>2</sub>O<sub>3</sub> (2054 °C), ZrO<sub>2</sub> (2700 °C), TiO<sub>2</sub> (1843 °C)] presents a challenge for plasma spray deposition of these three materials. However, an optimised process parameters chosen for each anode layers (Mo-Mo<sub>2</sub>C/Al<sub>2</sub>O<sub>3</sub>, Mo-Mo<sub>2</sub>C/ZrO<sub>2</sub>, Mo-Mo<sub>2</sub>C/TiO<sub>2</sub>) are (current: 500 A, voltage: 60-70 V, Argon gas: 42.08 lpm, H<sub>2</sub> gas flow: 34.2 lpm, carrier gas (Ar): 19.4 lpm, spray distance: 100 mm, powder feed rate: 70 g.min<sup>-1</sup>, spray angle: 60°), as listed in **Table 1**.

### *2.3 Microstructural Characterisation*

The surface characterisation of materials included scanning electron microscope (SEM) imaging using Karl Zeiss EVO LS10 and JEOL JSM 6010 LA, whereas, the elemental X-ray analysis (EDS) was done using Karl Zeiss EVO LS10 electron microscope. The X-ray diffraction (XRD) analysis using Rigaku MiniFlex 600 was used to reveal the crystalline phase composition of the coatings. Part of coating microstructure was investigated via

fracturing the coating flakes (by bending in a direction perpendicular to the coating surface) to reveal coating porosity and splat morphology. The total porosity of coating surface (on image acquired through SEM) was evaluated as the average of five area-normalized regions each from image analysis Infinity Analyze software (release 6.3, Lumenera Corporation). This software was used to measure pore size and number, providing the porous area distribution for each composition, and the pore area ratio (or fraction), defined as the sum of all pore areas divided by the total sample area analysed (e.g. **Fig. 3**). This was carried out using simple thresholding (at 65%) in the image analysis software. The threshold level was chosen manually so that the pore selection is not impaired or overestimated, and in this way it was possible to know the morphology of the pores. In addition, the porosity was also measured for one of the specimens using ImageJ program (release 1.49, public domain open source software), and the results were further compared. There can be other automated (e.g. programmable) techniques to measure pore fractions, threshold selection and sensitivity analysis which can be part of future development, implementation and investigation.

#### *2.4 Nanoindentation Testing*

The evaluation of hardness ( $H$ ) and elastic modulus ( $E_s$ ) of the coating cross-sections with substrate requires careful assessment of the test parameters. Nanoindentation hardness and elastic modulus measurements of the Hastelloy®X substrate were performed using a calibrated NanoTest™ system (Micromaterials Limited, UK) with a standard Berkovich tip. The measurements were taken in load control of 30 mN. The indentation procedures were programmed as three segments of trapezoidal shape. The first segment increased the load to a maximum value with a loading rate of 10 mN/s, followed by a 30-second holding segment at the maximum load. The third segment retrieved the indenter tip from the sample with an unloading rate of 10 mN/s.

As shown in **Fig. 4a**, twenty five measurements were performed on each coating polished cross-sections, which were distributed in five lines of 5 measurement points each, at a certain distance from the interface, from the coating surface [e.g. 16-17]. In preparation for the nanoindentation tests, specimens cross-section surface were ground and polished using diamond paste to avoid any effect of polishing which was expected to be broadly similar for all specimens [16-17]. Similarly, 10 measurements were performed on each substrate cross section near the interface (e.g. **Fig. 4b**), which were distributed in two lines of 5 measurement points each, at a certain distance from the interface. Indentations were spaced 22  $\mu\text{m}$ , to avoid any interaction between the sinking-in, piling-up, surface and subsurface lateral cracks of neighboring indentations. The  $P$ - $h$  profiles (e.g. **Fig. 4c**) were analysed using standard methods with the area function for the Berkovich indenter whereas the modulus and hardness were analysed according to Oliver and Pharr method [18]. Post-test residual impressions were mapped using an SEM. Nanoindentation tests were done in a temperature controlled instrument chamber at 300 K.

### 3. Results

#### 3.1 Anode Coating Porosity, Microstructure and Composition

In a representative example of image analysis using Infinity Analyze software (**Fig. 3**, shown here for APS coated Mo-Mo<sub>2</sub>C/ZrO<sub>2</sub> anode surface) for surface connected porosity measurement, the porous area is defined as the sum of all pore areas divided by the total sample area analysed (measured porosity of about 17%, **Fig. 3**). In addition, the porosity was also measured for this specimen using ImageJ program (measured porosity of about 19%), and the results were comparable. It can be seen that in scanning electron micrographs (**Fig. 5**) the presence of high surface connected porosity was observed on the coating surface (i.e. top view). We report herein that the anode layers of volumetric porosity as high as 19 $\pm$ 1% for

Mo-Mo<sub>2</sub>C/Al<sub>2</sub>O<sub>3</sub> (thickness: 250 μm) and Mo-Mo<sub>2</sub>C/TiO<sub>2</sub> (thickness: 300 μm) and around 16±1% for Mo-Mo<sub>2</sub>C/ZrO<sub>2</sub> (thickness: 220 μm), all controllable by a selection of the APS process parameters with no addition of a sacrificial pore-forming material.

In scanning electron micrographs (**Fig. 6**) the coating cross-sections (fractured) appears to indicate presence of high porosity for Mo-Mo<sub>2</sub>C/Al<sub>2</sub>O<sub>3</sub> and Mo-Mo<sub>2</sub>C/TiO<sub>2</sub>. An elemental analysis (as shown in **Fig. 7**) was performed in order to determine the distribution of the elements in different region of the anode coatings as shown in **Fig. 8**. The X-ray diffraction (XRD) analysis shown in **Fig. 9** was used to reveal the crystalline phase composition of the coatings.

### *3.2 Nanoindentation Testing*

Following the Oliver and Pharr method, the results of the nanoindentation testing are presented in **Fig. 10**. The hardness and elastic modulus values quoted are the averaged measurements which were performed on the coating surface, and on the lines distributed along the cross section in the coating and the lines along the cross section in the substrate [16-17]. The hardness results (**Fig. 10a**) indicate the upper layers of the coatings have higher values than the subsurface layers in coatings with some effect of the deposition on the substrate. The measurements of reduced elastic modulus (**Fig. 10b**) indicate that overall the values were very similar for each coatings with significantly high standard deviation in coating zones and low standard deviation in substrate zones.

## **4. Discussion**

### *4.1 Coating Microstructure*

The quality of an anode layer depends strongly on its microstructure. A high open porosity (surface connected) in combination with a good material distribution of Mo-Mo<sub>2</sub>C

and metal oxides (a)  $\text{Al}_2\text{O}_3$ , (b)  $\text{ZrO}_2$  and (c)  $\text{TiO}_2$  are demanded. The developed air plasma sprayed Mo-Mo<sub>2</sub>C/ $\text{Al}_2\text{O}_3$ , Mo-Mo<sub>2</sub>C/ $\text{ZrO}_2$  and Mo-Mo<sub>2</sub>C/ $\text{TiO}_2$  anode layers microstructures are shown in SEM micrographs. In micrographs (**Fig. 5**) mainly the presence of high surface connected porosity was observed. The other features include voids, unmolten particle, nonbonded intersplat areas, and cracks in splats (a distinct feature highlighted in **Fig. 5c**). It can also be observed that the surface connected porosity sizes were high (over 10  $\mu\text{m}$ ).

The total porosity of the anode layer coatings arises from voids created by partial melting of the agglomerate particles as well as the presence of interlamellar and intralamellar cracks. Porosity is further introduced upon subsequent reduction of the deposited powders as well as from the addition of sacrificial pore-forming materials to the feedstock [19]. We report herein that anode layers of about 200  $\mu\text{m}$  to 300  $\mu\text{m}$  thicknesses and volumetric porosity as high as 20% is controllable by a selection of the APS process parameters with no addition of a sacrificial pore-forming material.

The reduced thickness (about 300  $\mu\text{m}$  through thermal spraying as opposed to high thickness due to casting) and high surface connected porosity of anode layer can potentially lead to an increment of gas permeability through a system of pores and it can also results in a high flux of fuel to the anode/electrolyte interface and of the produced  $\text{H}_2\text{O}$  away from this interface. However, further characterisation of the combined microstructure (including electrolyte and cathode) and its parameters, e.g. total porosity, open porosity, pore size distribution, as well as gas permeability can be used as control parameters for the development of highly permeable anode material. Despite the potential benefits that thermal spray processing can offer in SOFC technology, significant challenges still remain in the development of thermal spray processing (e.g. some un-molten powder particles, **Fig. 5**) in comparison to the SOFC wet ceramic production. Generally speaking, coatings deposited by APS have a porosity ranging from 5 vol.% to 15 vol.%, which is much less than the desired

porosity level of approximately 30 to 40 vol.% (achievable through wet ceramic production routes, e.g. tape casting, screen printing, and co-sintering) required for high-gas diffusivity within SOFC anodes [5]. Also, for other combination of anode materials, through literature it is also known that additional porosity is produced during NiO reduction to Ni, which generally elevates the porosity by approximately 20 vol.%, depending on the NiO content in the anode precursor [5].

As shown in **Fig. 6** (fractured coating cross-section surfaces), the splat thickness and features within appears to be different for Mo-Mo<sub>2</sub>C/Al<sub>2</sub>O<sub>3</sub> compared to Mo-Mo<sub>2</sub>C/ZrO<sub>2</sub> and Mo-Mo<sub>2</sub>C/TiO<sub>2</sub> anode layers coatings. The splats for Mo-Mo<sub>2</sub>C/Al<sub>2</sub>O<sub>3</sub> anode layers coatings appear more lamellar but less cohesive (layer gaps between splats), whereas, for Mo-Mo<sub>2</sub>C/ZrO<sub>2</sub> and Mo-Mo<sub>2</sub>C/TiO<sub>2</sub> anode layers coatings, the splat lamellar features were not clear and were more cohesive. The difference in splat and associated features between Mo-Mo<sub>2</sub>C/Al<sub>2</sub>O<sub>3</sub> and Mo-Mo<sub>2</sub>C/ZrO<sub>2</sub> or Mo-Mo<sub>2</sub>C/TiO<sub>2</sub> anode layers coatings may be due to different powder sizes (nominal particle size distribution for Al<sub>2</sub>O<sub>3</sub>: -31+3.9 μm, ZrO<sub>2</sub>: -100+325 μm, TiO<sub>2</sub>: -105+32 μm), especially when all depositions were carried out at the same APS process parameters. As was seen in **Fig. 5c**, the constraining of splats (though very few) may have led to the formation of submicroscopic vertical cracks of splats and their coalescence resulted in typical brittle failure for Mo-Mo<sub>2</sub>C/TiO<sub>2</sub> anode layer coating. Such vertical cracks of splats were not observed for Mo-Mo<sub>2</sub>C/Al<sub>2</sub>O<sub>3</sub> and Mo-Mo<sub>2</sub>C/ZrO<sub>2</sub> anode layers coatings. The Mo-Mo<sub>2</sub>C/TiO<sub>2</sub> anode layer coatings (**Figs. 6(I)c**) appear to have fewer gaps or voids between splats, indicating relatively higher bond strength. Layering as shown in **Figs. 6(II)** may be a result of the density difference of the two feedstocks or differences in the trajectory of particle flow in the plasma. It is also possible that the formation of distinct separate layers may occur due to powder clogging (e.g. due to different geometry of the powders). The well-mixed areas may be a result of a localized disturbance affecting the

deposition of either feedstock, such as an underlying surface feature leading to localised surface roughness [20].

#### 4.2 Coating Morphology

An elemental analysis (**Fig. 7**) was performed on the air plasma sprayed Mo-Mo<sub>2</sub>C/Al<sub>2</sub>O<sub>3</sub>, Mo-Mo<sub>2</sub>C/ZrO<sub>2</sub> and Mo-Mo<sub>2</sub>C/TiO<sub>2</sub> anode materials in order to determine the distribution (**Fig. 8**) of the elements in different region of the coatings. It confirms the presence of various expected elements in each anode layer coatings, mainly dominated by molybdenum in Mo<sub>2</sub>C/Al<sub>2</sub>O<sub>3</sub>, Mo-Mo<sub>2</sub>C/ZrO<sub>2</sub>, and combination of molybdenum and titanium in Mo-Mo<sub>2</sub>C/TiO<sub>2</sub> anode layers. The **Fig. 7** summarize element and atomic weight percentage for each anode types.

In the XRD of air plasma sprayed Mo-Mo<sub>2</sub>C/Al<sub>2</sub>O<sub>3</sub> anode layer coatings (**Fig. 9a**), separate peaks are identified for Mo and C; it is clear that there was solid state reaction between Mo-Mo<sub>2</sub>C and Al<sub>2</sub>O<sub>3</sub>. The formation of secondary phase Al<sub>2</sub>Mo<sub>3</sub>C (known to be superconductor [21]) due to interaction between Mo-Mo<sub>2</sub>C and Al<sub>2</sub>O<sub>3</sub> is observed. As shown in **Fig. 6** (column II, polished cross-section of SEM micrographs), overall, it can be seen that each anode coating forms distinct alternating layers of the two materials (identifiable largely by lighter grey molybdenum and also darker grey other lamellar structures, different but indicative metal-oxide component for each feedstock used) in each anode coatings. In polished cross-section of Mo-Mo<sub>2</sub>C/Al<sub>2</sub>O<sub>3</sub> anode layer, it can be seen that apart from distinct alternating layers of the two materials, interconnected pore density (largely due to fused and crushed Al<sub>2</sub>O<sub>3</sub>, with original particle size distribution of -31+3.9 μm) are of smaller sizes and evenly spread.

In the case for Mo-Mo<sub>2</sub>C/ZrO<sub>2</sub> anode layer coatings (**Fig. 9b**), separate peaks are identified for Mo but not for C; it is clear that there is not any solid state reaction between

Mo-Mo<sub>2</sub>C and ZrO<sub>2</sub> (suggesting no incorporation of Zr into the crystalline lattice of Mo<sub>2</sub>C [19]). In polished cross-section of Mo-Mo<sub>2</sub>C/ZrO<sub>2</sub> anode layer, it can be seen that apart from distinct alternating layers of the two materials, interconnected pore density (largely due to fused and crushed ZrO<sub>2</sub>, with original particle size distribution of -100+325 μm) is relatively higher (and of large sizes and evenly spread) compared to other two anode layers.

In the case for Mo-Mo<sub>2</sub>C/TiO<sub>2</sub> anode layer coatings (**Fig. 9c**), separate peaks are identified for Mo and MoC; it is clear that there is not any solid state reaction between Mo-Mo<sub>2</sub>C and TiO<sub>2</sub>. In polished cross-section of Mo-Mo<sub>2</sub>C/TiO<sub>2</sub> anode layer, it can be seen that apart from distinct alternating layers of the two materials, interconnected pore density (largely due to agglomerated/sintered and spheroidal TiO<sub>2</sub>, with original particle size distribution of -105+32 μm) are of smaller sizes and evenly spread.

In all these cross-sectional morphologies, the molybdenum appears to be much more melted forming thicker splats, and porosity is made up of regions between the lamellae and connected networks of globular pores. Pores in each of the deposited coatings consist of voids (large voids clearly seen in **Fig. 6(IIb)**) and small two-dimensional voids such as the interlamellar non-bonded interfaces and microcracks in individual lamellae. These pores are therefore interconnected through microcracks in individual splats in the anode, which can permit the passage of gas through the anode. However, these inhomogeneous layer might affect the anode performance by modifying ohmic and activation losses, and, further investigations are needed.

#### *4.3 Nanohardness and Elastic Modulus*

The nanohardness results (**Fig. 10a**) indicate the upper layers of the coatings have higher average values than the subsurface layers in coatings with some effect of the APS high temperature deposition on the substrate (higher bound at the interface). However, the little

difference in the average hardness can be attributed to the considerably lower degree of phase transformation in APS Mo-Mo<sub>2</sub>C/ZrO<sub>2</sub> or Mo-Mo<sub>2</sub>C/TiO<sub>2</sub> deposition (**Fig. 9**). This could also lead to potential differences between the measured elastic values. However, other factors such as intersplat bonding (cohesive strength), residual stress and porosity also contributed to the differences in the elastic modulus of three anode layer coatings. The measurements of reduced elastic modulus (**Fig. 10b**) indicate that overall the values were very similar for each coatings with significantly high standard deviation in coating zones and low standard deviation in substrate zones. However, the measured reduced elastic modulus does not suggest that the top layers of three coating had a higher elastic modulus than their subsurface layers. High standard deviations in through thickness nanoindentation measurements (hardness, reduced elastic modulus) also suggest a significant effect of the complex anode coating morphology [16-17].

The elastic modulus results of the substrate, near the coating-substrate interface, suggest that the spraying conditions using APS had a slight change in the average modulus values, but falls within the standard deviation range between coating materials. Also, the higher magnification images of the Hastelloy®X substrate near the interface indicated negligible differences in the microstructure. The hardness did not show significant differences between the near-interface hardness of the Hastelloy®X substrate between the coating materials, indicating that microstructural transformation was not significant, which will be consistent with the observed microstructure. Hence, it is difficult to relate this little change in modulus and no change in nanohardness of near-interface modulus of Hastelloy®X on possible microstructural transformations in Hastelloy®X during APS coating deposition. It has been indicated that elastic modulus measurement can be influenced by residual stress, which can be attributed to the differences in the real and measured indentation contact areas

[16-17]. Hence, as the hardness is calculated based on the area of contact and modulus slope of the unloading curve, they do not follow similar trends in the near interface substrate region.

#### *4.4 Molybdenum Carbide Based SOFC Anode Properties*

The anode is probably the most delicate functional layer of an SOFC with regard to the requirements it has to fulfil. On the one hand its electrical conductivity has to be as high as possible to minimize electric losses and supply electrons [22]. In this investigation commercially available carbide of molybdenum powder catalyst (Mo-Mo<sub>2</sub>C) and three metal oxides (e.g. Al<sub>2</sub>O<sub>3</sub>, ZrO<sub>2</sub>, TiO<sub>2</sub>, all beneficial for catalyst stability) were used to prepare three composite feedstock powders (Mo-Mo<sub>2</sub>C/Al<sub>2</sub>O<sub>3</sub>, Mo-Mo<sub>2</sub>C/ZrO<sub>2</sub>, Mo-Mo<sub>2</sub>C/TiO<sub>2</sub>) to fabricate three different SOFC anodes. The anode electrical conductivity tests which were carried for temperature between room temperature to 800 °C (or 1073 K) using a VersaSTAT3-400 (Ametek) electrochemical impedance spectra (EIS). There are no literature to compare the conductivity results for such material compositions, but it can be seen in **Fig. 11** that the conductivity of anode first increases and then decreases with the increase in temperature. All the three specimens show similar trends, among all specimen Mo-Mo<sub>2</sub>C/ZrO<sub>2</sub> shows high value of conductivity overall and at about 800 °C. Between 220 °C to 360 °C sharp increase in conductivity has been observed for all three specimens, after that the conductivity decreased as temperature increased, which indicates the metallic nature of substrates. There may be some agglomeration of particles due to sintering but it is not the only reason for decrease in conductivity as particles are relatively connected to each other. Since the experimental data on Mo conductivity is not available, there can be percolating network of Mo, which is responsible for conductivity; simultaneously there could be contribution of Al<sub>2</sub>O<sub>3</sub>, TiO<sub>2</sub> and ZrO<sub>2</sub> towards increase in conductivity.

Further it is reported that Mo-Mo<sub>2</sub>C and metal oxides (Al<sub>2</sub>O<sub>3</sub>, ZrO<sub>2</sub> and TiO<sub>2</sub>) would interact with each other and transfer of electron from Mo-Mo<sub>2</sub>C to vacant oxygen site in Al<sub>2</sub>O<sub>3</sub>, ZrO<sub>2</sub> and TiO<sub>2</sub> would take place leading to strong metal support interaction (SMSI) [23]. Perhaps SMSI effect leads to decrease in Mo-Mo<sub>2</sub>C coarsening with the increase in temperature and thus conductivity remains largely unchanged for all three anodes with the increase in temperature. It is also known that Mo metal forms a low melting and high volatile oxide which rapidly consumes the metal when exposed to air at temperatures above 1063 K, a condition which can be better by alloying [24] (i.e. through Mo-Mo<sub>2</sub>C system) in the current SOFC application with various metal oxides (e.g. Al<sub>2</sub>O<sub>3</sub>, ZrO<sub>2</sub> and TiO<sub>2</sub>), however, further investigations are needed.

#### *4.5 Future Prospects*

To improve SOFC anode porosity, further development can focus on the usage of alternative powders (fine or nanostructured), the application of pore formers (carbon or starch), and further optimization of the spray parameters. While cost and performance of SOFCs remain major barriers to their widespread use, thermal spray processing has the potential to drastically reduce these barriers by rapidly increasing production rates and reducing capital equipment, materials, and SOFC system cost. It has also the potential to increase performance by the use of graded composition and microstructures, and by rapidly solidifying fine microstructures with good adhesion to the substrate and no microstructure coarsening due to sintering [5]. It is anticipated that microstructures of fine or nanostructured powders in particular will be of considerable interest for use in SOFCs due to their potential to increase the surface area of active sites on which the electrode reactions take place, thereby improving reaction kinetics.

The capability of plasma processing to fabricate fine powders can be an area of interest. A feature of such fine powder is the high fraction of atoms that reside at grain boundaries and grain surfaces, largely enhancing the chemical activity. An extended reaction surface area with an optimized porous microstructure is expected to enhance the electrode performance [5]. This technique has recently been employed as an alternative processing route for SOFC fabrication, including component deposition and powder production. Some researcher [25] have demonstrated the feasibility of synthesizing nanopowders (e.g. Zn: 15 nm, Fe-Ti: 32 nm, Ni-Al: 16.4 nm, WO<sub>3</sub>: 16.1 nm, CeO<sub>2</sub>: 18.6 nm, SiC: 28 nm, MoO<sub>3</sub>: 14 nm, Ni-B: 12.8 nm, CaO: 14.8 nm mean sizes, etc.) directly from liquid precursors. These examples demonstrate the feasibility and effectiveness of the principles of the invention in producing nanosize powders from micron-sized precursors, and which can be implemented to prepare various other composite feedstock for potential application in SOFC electrode (anode: porous layer, electrolyte: dense layer, cathode: porous layer) deposition using beyond conventional thermal spray techniques (such as suspension HVOF [26] and suspension plasma spraying [22]). Moreover, the introduction of carbon or other pore formers to the feedstock powder can induce a significant increment of the porosity after the pore formers are burnt out (e.g. by annealing in air) [27].

## 5. Conclusions

The development of stoichiometric carbon free molybdenum carbide based anode layer with Al<sub>2</sub>O<sub>3</sub>, ZrO<sub>2</sub> and TiO<sub>2</sub> metal oxides, prepared by air plasma technique, has been demonstrated. Thermal spraying process can enable the control of porosity in SOFCs which can be used to control gas permeability in anode layer. It is concluded that the three optimized anode layers of thicknesses between 200 to 300 μm and porosity as high as 20% for Mo-Mo<sub>2</sub>C/Al<sub>2</sub>O<sub>3</sub> (250 μm thick) and Mo-Mo<sub>2</sub>C/TiO<sub>2</sub> (300 μm thick) and around 17% for Mo-

Mo<sub>2</sub>C/ZrO<sub>2</sub> (220 μm thick), all controllable by a selection of the APS process parameters with no addition of sacrificial pore-forming material. The nanohardness results indicate the upper layers of the coatings have higher values than the subsurface layers in coatings with some effect of the deposition on the substrate. The total porosity can be further increased through the addition of sacrificial pore-forming materials such as graphitic carbon or potato starch and also through inclusion of a pore former in aqueous suspension (using suspension thermal spray techniques), in addition to the porosity introduced in the current work. Overall each anode coating forms distinct alternating layers of the two materials. In Mo-Mo<sub>2</sub>C/Al<sub>2</sub>O<sub>3</sub> and Mo-Mo<sub>2</sub>C/TiO<sub>2</sub> anode layers, the interconnected pore density are of smaller sizes, whereas, in Mo-Mo<sub>2</sub>C/ZrO<sub>2</sub> anode layer, the interconnected pore density is relatively higher (and of large sizes) compared to other two anode layers. Therefore, the process parameters developed through this work paves a way for further development of other composite layers. The microstructures and basic electrochemical properties of the anode coatings (e.g. Mo-Mo<sub>2</sub>C/ZrO<sub>2</sub> shows high value of electrical conductivity overall and at about 800 °C) were analysed which showed features consistent with the desired properties.

### **Acknowledgement**

This work has been supported by the project titled “Advance anode materials for direct hydrocarbon proton conducting solid oxide fuel cell (PC-SOFC) in auxiliary power unit”, funded by Saudi Aramco (Contract number 6000074197).

### **References**

- [1] Hydrogen & Fuel Cells: Review of National R&D Programs, International Energy Agency, 2004.

- [2] S. McIntosh, R.J. Gorte, Direct hydrocarbon solid oxide fuel cells, *Chem. Rev.* 104, 2004, p. 4845-4865.
- [3] Z. Shao, S.M. Haile, J. Ahn, P.D. Ronney, Z. Zhan, S. A. Barnett, A thermally self-sustained micro solid-oxide fuel-cell stack with high power density, *Nature*, 435, 9<sup>th</sup> June 2005, p. 795-798.
- [4] F. Tietz, H. P. Buchkremer, D. Stöver, 10 years of materials research for solid oxide fuel cells at forschungszentrum jülich, *Journal of Electroceram*, 17, 2006, p. 701-707.
- [5] R. Hui, Z. Wang, O. Kesler, L. Rose, J. Jankovic, S. Yick, R. Maric, D. Ghosh, Thermal plasma spraying for SOFC's: Applications, potential advantages, and challenges, *Journal of Power Sources*, 170, 2007, p. 308-323.
- [6] K. C. Wincewicz, J.S. Cooper, Taxonomies of SOFC material and manufacturing alternatives, *Journal of Power Sources*, 140, 2005, p. 280-296.
- [7] S.M. Haile, Fuel cell materials and components, *Acta Materialia*, 51, 2003, p. 5981-6000.
- [8] B.D. White, O. Kesler, L. Rose, Air plasma spray processing and electrochemical characterization of SOFC composite cathodes, *Journal of Power Sources*, 178, 2008, p. 334-343.
- [9] P. Heo, K. Ito, A. Tomita, T. Hibino, A proton-conducting fuel cell operating with hydrocarbon fuel, *Angewandte Chemie*, 47, 2008, p. 7841-7844.
- [10] Fuel cells: Hydrocarbons versus hydrogen, *Nature Asia*, 03 December 2008,
- [11] A. J. Brungs, A. P. E. York, J. B. Claridge, C. M. Alvarez, M. L. H. Green, Dry reforming of methane to synthesis gas over supported molybdenum carbide catalyst, *Catalysis Letters*, 70, 2000, p. 117-122.
- [12] P. Liu, J. A. Rodriguez, Catalytic properties of molybdenum carbide, nitride and phosphide: a theoretical study, *Catalysis Letters*, 91, 2003, p. 247-252.

- [13] T. Hyeon, M. Fang, K. S. Suslick, Nanostructured molybdenum carbide: Sonochemical synthesis and catalytic properties, *Journal of American Chemical Society*, 118, 1996, p. 5492-5493
- [14] E. Drozd, The influence of the method of addition of  $\text{Al}_2\text{O}_3$  to 3YSZ material on its thermal and electrical properties, *Journal of Thermal Analysis and Calorimetry*, 118, 2014, p. 1345-1353.
- [15] Jianghong Gong, Ying Li, Zilong Tang, Zhongtai Zhang, Enhancement of the ionic conductivity of mixed calcia/yttria stabilized zirconia, *Materials Letters*, 46, 2000, p. 115-119.
- [16] R. Ahmed, N. H. Faisal, A. M. Paradowska, M. Fitzpatrick, K. A. Khor, Neutron diffraction residual strain measurements in nanostructured hydroxyapatite coatings for orthopaedic implants, *Journal of the Mechanical Behavior of Biomedical Materials*, 4(8), 2011, p. 2043-2054
- [17] R. Ahmed, N. H. Faisal, A. M. Paradowska, M. Fitzpatrick, Residual strain and fracture response of  $\text{Al}_2\text{O}_3$  coatings deposited via APS and HVOF techniques, *Journal of Thermal Spray Technology*, 21(1), 2012, p. 23-40
- [18] W. C. Oliver, G. M. Pharr, An improved technique for determining hardness and elastic modulus using load and displacement sensing indentation experiments. *Journal of Materials Research*, 7, 1992, p. 1564-1583.
- [19] C. Metcalfe, J. Harris, J. Kuhn, M. Marr, O. Kesler, Progress in metal-supported axial-injection plasma sprayed solid oxide fuel cells using nanostructured NiO- $\text{Y}_{0.15}\text{Zr}_{0.85}\text{O}_{1.925}$  dry powder anode feedstock, *Journal of Thermal Spray Technology*, 22(5), 2013, p. 599-608.
- [20] M. Cuglietta, J. Kuhn, O. Kesler, A novel hybrid axial-radial atmospheric plasma spraying technique for the fabrication of solid oxide fuel cell anodes containing Cu,

- Co, Ni, and Samaria-Doped Ceria, *Journal of Thermal Spray Technology*, 22(5), 2013, p. 609-621.
- [21] K. S. Weil, Analysis of the structure and magnetic properties of new multicomponent transition metal nitride compounds, *The Electrochemical Society's Interface*, Winter 1998, p. 49-51.
- [22] D. Soysal, J. Arnold, P. Szabo, R. Henne, S. A. Ansar, Thermal plasma spraying applied on solid oxide fuel cells, *Journal of Thermal Spray Technology*, 22(5), 2013, p. 588-598.
- [23] P. Heo, M. Nagao, M. Sano, T. Hibino, A high-performance Mo<sub>2</sub>C-ZrO<sub>2</sub> anode catalyst for intermediate-temperature fuel cells, *Journal of The Electrochemical Society*, 154, 2007, p. B53-B56.
- [24] J. J. Liao, R. C. Wilcox, R. H. Lee, Structures and properties of the Mo-Mo<sub>2</sub>C system, *Scripta Metallurgica et Materialia*, 24, 1990, p. 1647-1652.
- [25] S. Pirzada, T. Yadav, Integrated thermal process for the continuous synthesis of nanoscale powders, US Patent 5,851,507 A (1998).
- [26] R. Ahmed, N. H. Faisal, Nayef M. Al-Anazi, S. Al-Mutairi, F.-L. Toma, L.-M. Berger, A. Potthoff, Y. O. Elakwah, M. F. A. Goosen, Structure property relationship of suspension thermally sprayed WC-Co nanocomposite coatings, *Journal of Thermal Spray Technology*, 24(3), 2014, p. 357-377.
- [27] L.-W. Tai, P. A. Lessing, Plasma spraying of porous electrodes for a planar solid oxide fuel cell, *Journal of American Ceramic Society*, 74(3), 1991, p. 501-504.

## Table caption

**Table 1.** APS thermal spray process parameters

## Figure captions

**Fig. 1.** SOFC component assembly.

**Fig. 2.** (a) Agglomerated and sintered Mo-Mo<sub>2</sub>C powder showing high porosity and surface area, (b) disc specimens holder in circular holes which were cut on steel plate and then mounted on jaw chuck, and (c) SOFC anode thermal spraying manufacturing in industrial coating chamber: discs after assembly in circular holes which are cut on steel plate.

**Fig. 3.** Representative example for porosity measurement: (a) SEM image of Mo-Mo<sub>2</sub>C/ZrO<sub>2</sub> anode layer showing surface connected porosities, (b) selected porous zone, and (c) measured porosity of about 17% (defined as the sum of all pore areas divided by the total sample area analysed).

**Fig. 4.** Berkovich nanoindentation tests: (a) Through thickness measurement scheme, (b) indent line shown here for specimen Mo-Mo<sub>2</sub>C/ZrO<sub>2</sub> (white inclusions shown below the interface are some debris), and (c) force-displacement profiles.

**Fig. 5.** SEM images of APS coated anode layer surfaces showing surface connected porosities and unmolten powder particles: (a) Mo-Mo<sub>2</sub>C/Al<sub>2</sub>O<sub>3</sub>, (b) Mo-Mo<sub>2</sub>C/ZrO<sub>2</sub> and (c) Mo-Mo<sub>2</sub>C/TiO<sub>2</sub>.

**Fig. 6.** SEM images of APS coated anode layer cross-section surfaces: (a) Mo-Mo<sub>2</sub>C/Al<sub>2</sub>O<sub>3</sub>, (b) Mo-Mo<sub>2</sub>C/ZrO<sub>2</sub> and (c) Mo-Mo<sub>2</sub>C/TiO<sub>2</sub>

**Fig. 7.** EDX of APS coated anode layers: (a) Mo-Mo<sub>2</sub>C/Al<sub>2</sub>O<sub>3</sub>, (b) Mo-Mo<sub>2</sub>C/ZrO<sub>2</sub> and (c) Mo-Mo<sub>2</sub>C/TiO<sub>2</sub>.

**Fig. 8.** EDX (elemental distribution or mapping) of APS coated anode materials: (a) Mo-Mo<sub>2</sub>C/Al<sub>2</sub>O<sub>3</sub>, (b) Mo-Mo<sub>2</sub>C/ZrO<sub>2</sub> and (c) Mo-Mo<sub>2</sub>C/TiO<sub>2</sub>.

**Fig. 9.** XRD of APS coated anode layers (coating surface): (a) Mo-Mo<sub>2</sub>C/Al<sub>2</sub>O<sub>3</sub>, (b) Mo-Mo<sub>2</sub>C/ZrO<sub>2</sub> and (c) Mo-Mo<sub>2</sub>C/TiO<sub>2</sub>.

**Fig. 10.** Nanoindentation results (hardness and elastic modulus) of APS coated anode layer specimens (Mo-Mo<sub>2</sub>C/Al<sub>2</sub>O<sub>3</sub>, Mo-Mo<sub>2</sub>C/ZrO<sub>2</sub> and Mo-Mo<sub>2</sub>C/TiO<sub>2</sub>) on Hastelloy<sup>®</sup>X substrates.

**Fig. 11.** Electrical conductivity variation with temperature: APS coated anode layer on Hastelloy<sup>®</sup>X substrate [Mo-Mo<sub>2</sub>C/Al<sub>2</sub>O<sub>3</sub>, Mo-Mo<sub>2</sub>C/ZrO<sub>2</sub> and Mo-Mo<sub>2</sub>C/TiO<sub>2</sub>].

**Table 1.** APS thermal spray process parameters

<b>Process parameter</b>	<b>Anode coating</b>
Materials	Mo-Mo <sub>2</sub> C:Al <sub>2</sub> O <sub>3</sub> ::0.8:0.2 Mo-Mo <sub>2</sub> C:ZrO <sub>2</sub> ::0.8:0.2 Mo-Mo <sub>2</sub> C:TiO <sub>2</sub> ::0.8:0.2
Current	500 A
Voltage	60-70 V
Primary gas (Argon)	100 psi (0.68 MPa); 42.08 lpm
Secondary gas (Hydrogen)	50 psi (0.34 MPa); 34.2 lpm
Carrier gas (Argon)	100 psi (0.68 MPa); 19.4 lpm
Standoff distance	100 mm
Feed rate	70 g/min
Spray angle	60°
Coating thickness	200 to 300 μm
APS gun	Metco 3MB gun
APS nozzle	Metco 3M7A-GP (small bore)

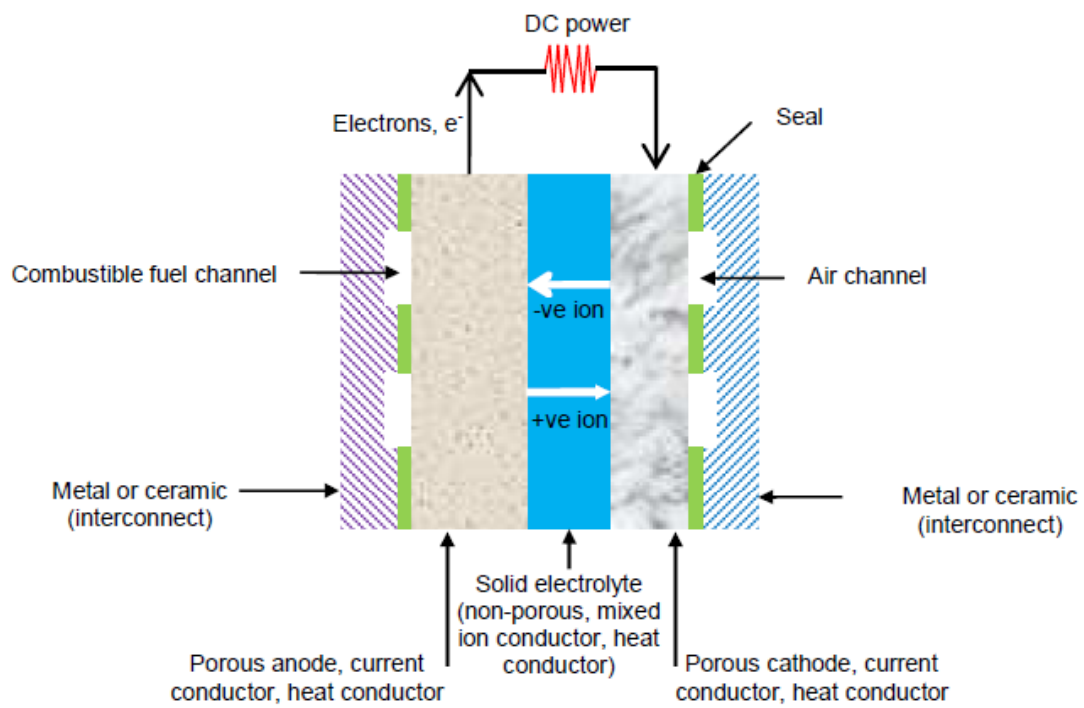


**Fig. 1.** SOFC component assembly.

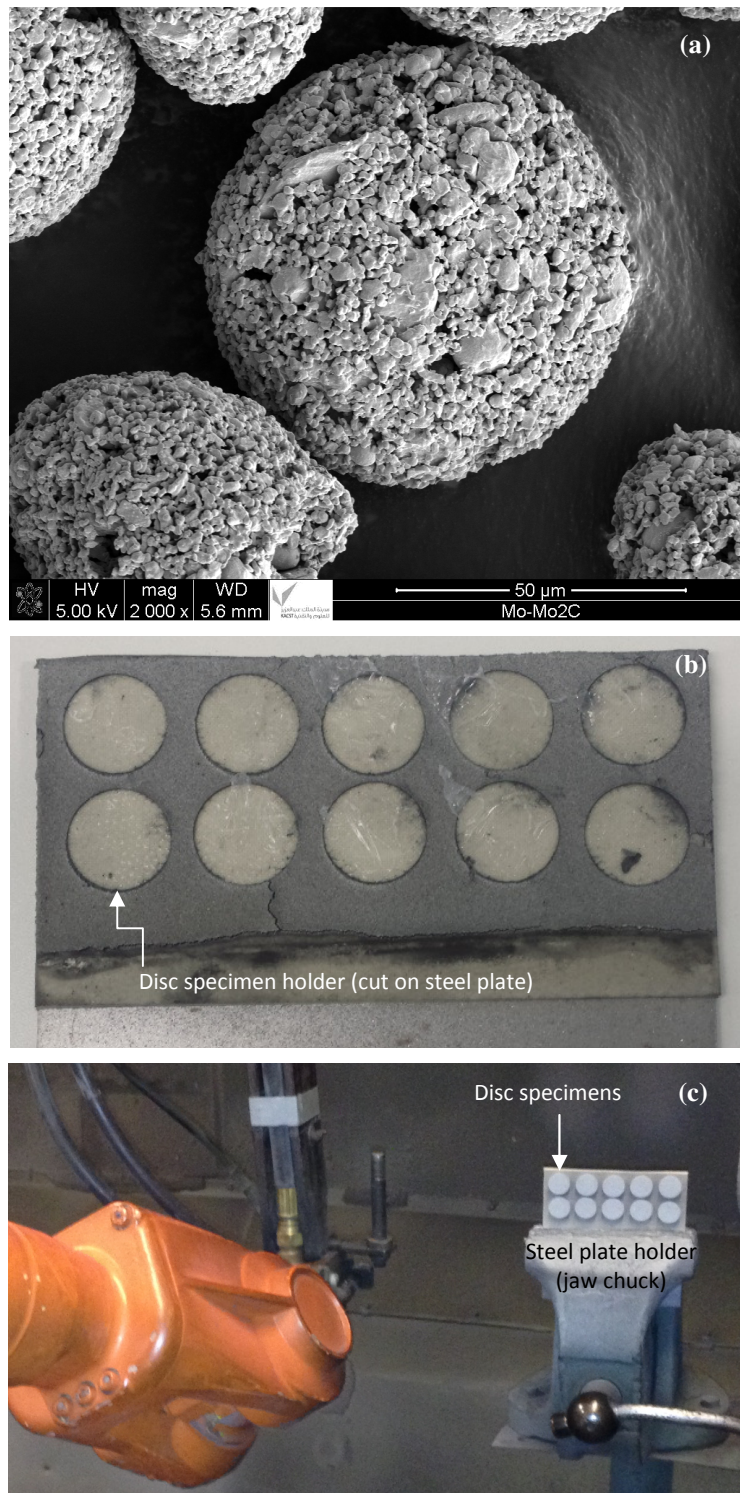


**Fig. 2.** (a) Agglomerated and sintered Mo-Mo<sub>2</sub>C powder showing high porosity and surface area, (b) disc specimens holder in circular holes which were cut on steel plate and then mounted on jaw chuck, and (c) SOFC anode thermal spraying manufacturing in industrial coating chamber: discs after assembly in circular holes which are cut on steel plate.

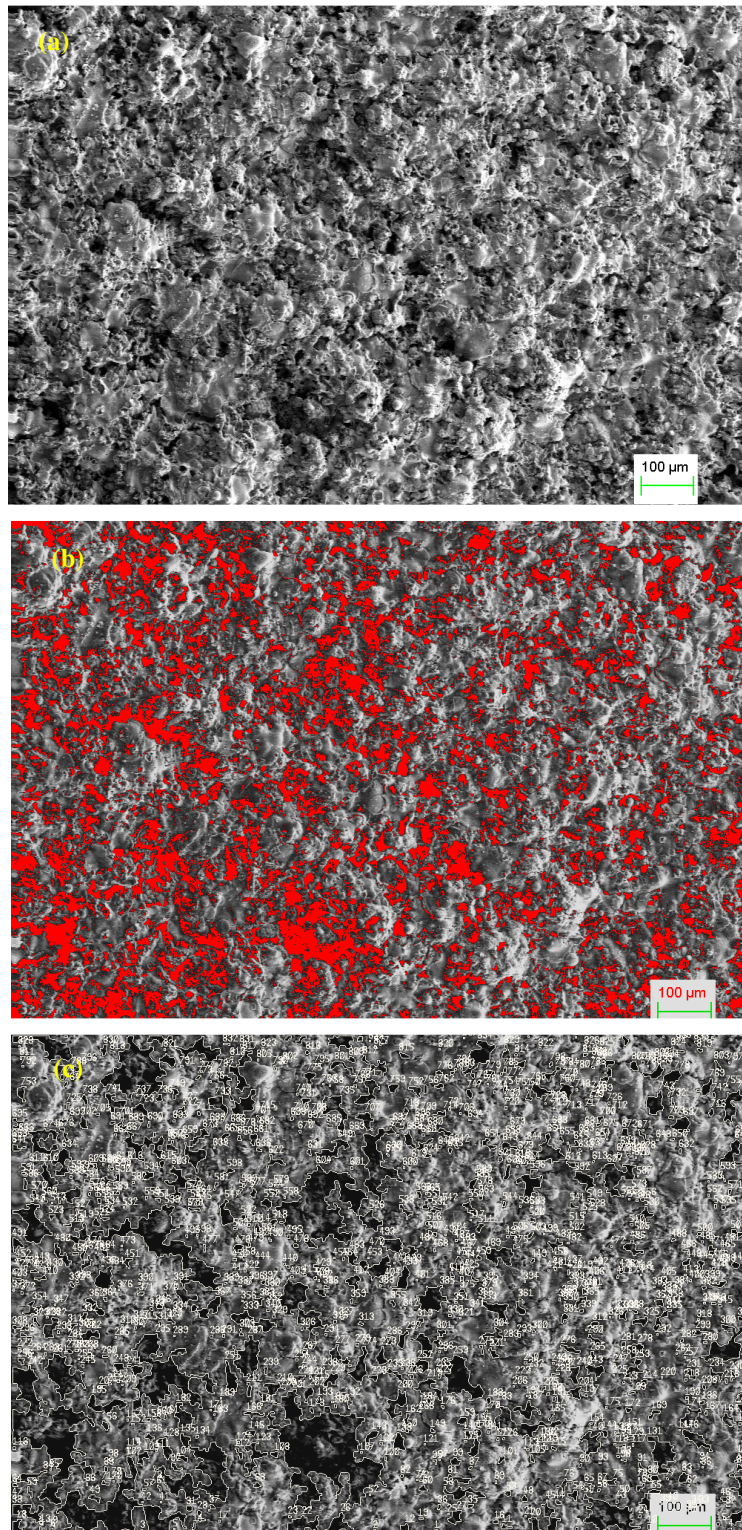


**Fig. 3.** Representative example for porosity measurement: (a) SEM image of Mo-Mo<sub>2</sub>C/ZrO<sub>2</sub> anode layer showing surface connected porosities, (b) selected porous zone, and (c) measured porosity of about 17% (defined as the sum of all pore areas divided by the total sample area analysed).

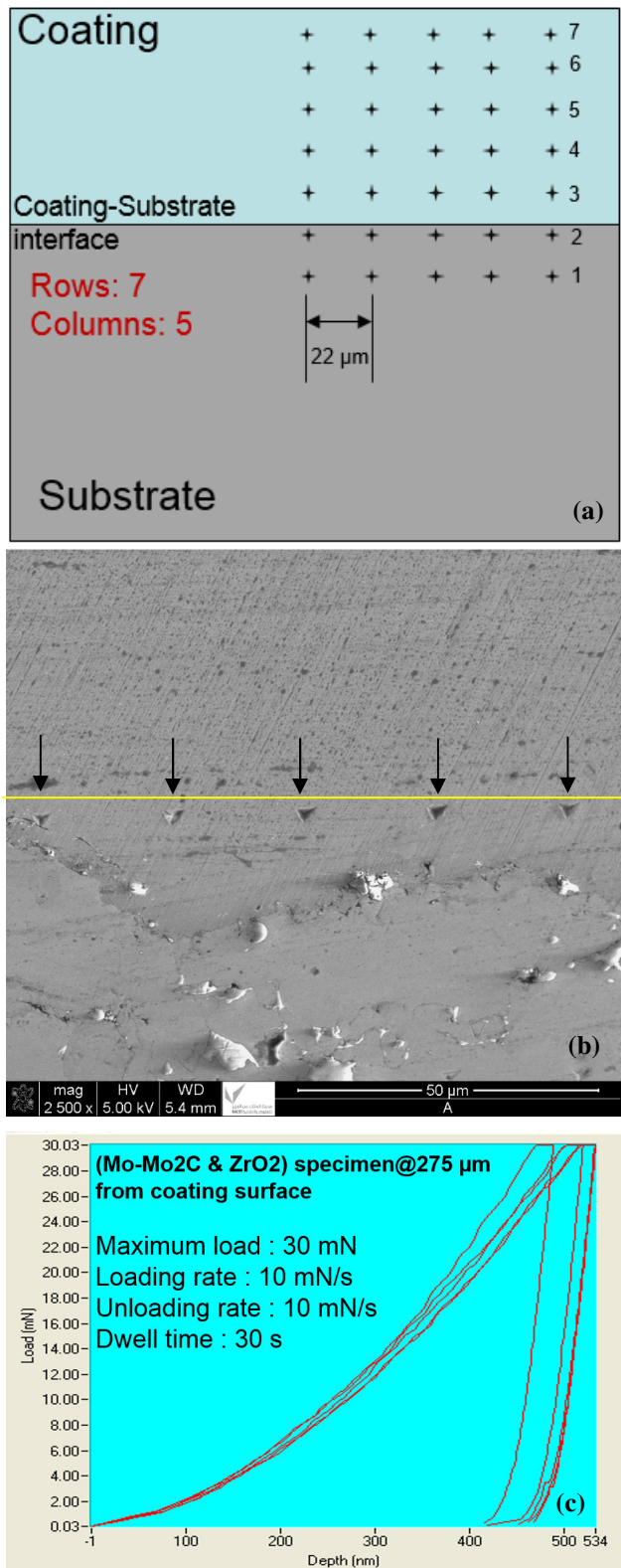


**Fig. 4.** Berkovich nanoindentation tests: (a) Through thickness measurement scheme, (b) indent line shown here for specimen Mo-Mo<sub>2</sub>C/ZrO<sub>2</sub> (white inclusions shown below the interface are some debris), and (c) force-displacement profiles.

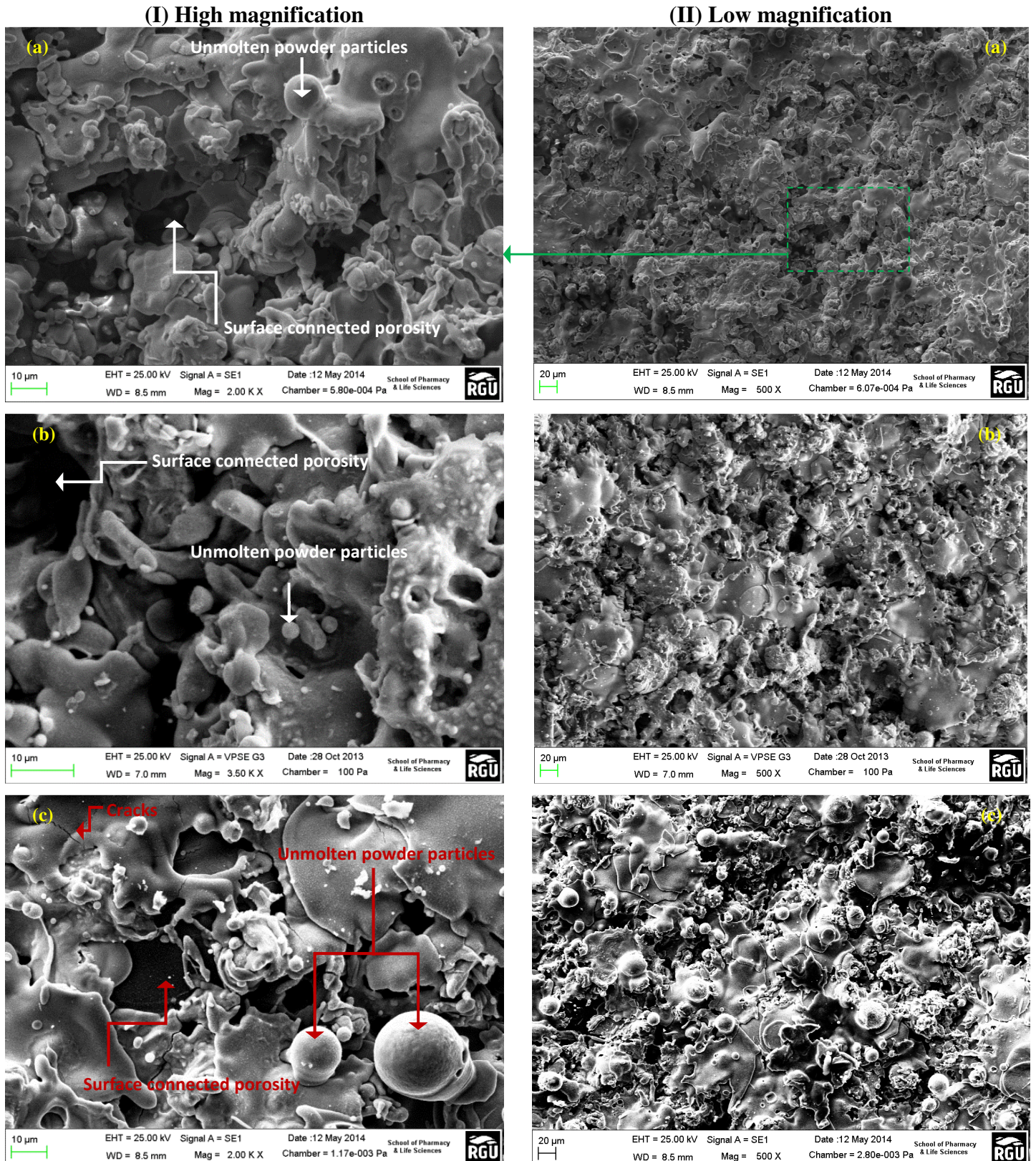
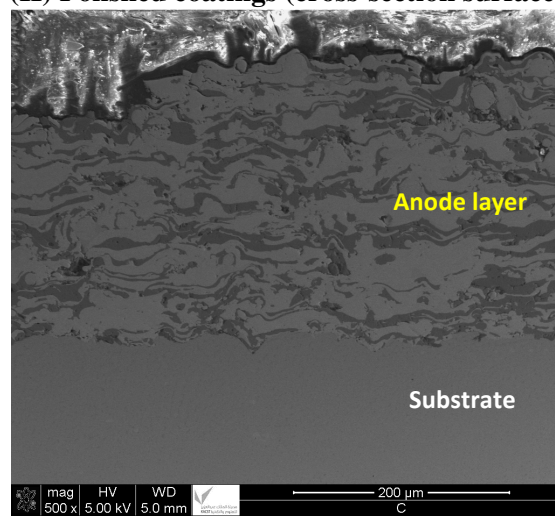
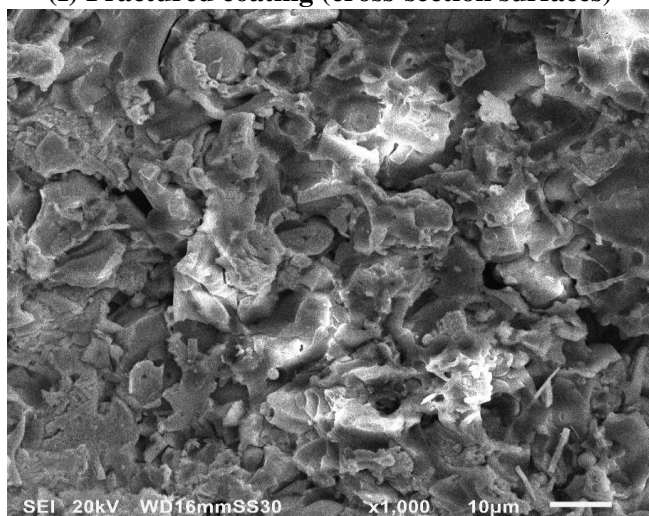


**Fig. 5.** SEM images of APS coated anode layer surfaces showing surface connected porosities and unmolten powder particles: (a) Mo-Mo<sub>2</sub>C/Al<sub>2</sub>O<sub>3</sub>, (b) Mo-Mo<sub>2</sub>C/ZrO<sub>2</sub> and (c) Mo-Mo<sub>2</sub>C/TiO<sub>2</sub>.

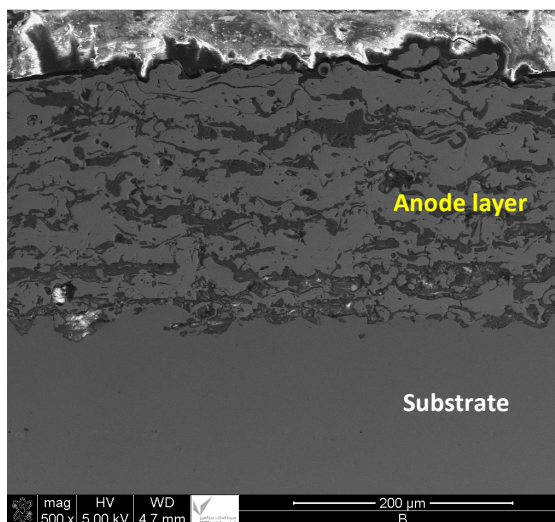
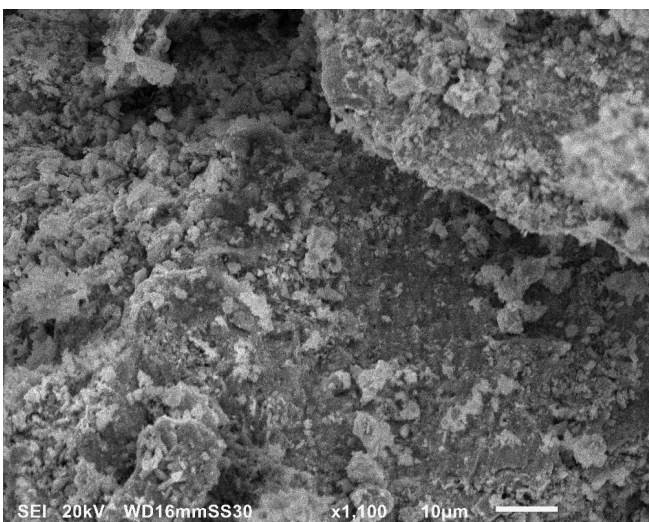
(I) Fractured coating (cross-section surfaces)

(II) Polished coatings (cross-section surface)

(a) Mo-Mo<sub>2</sub>C/Al<sub>2</sub>O<sub>3</sub>



(b) Mo-Mo<sub>2</sub>C/ZrO<sub>2</sub>



(c) Mo-Mo<sub>2</sub>C/TiO<sub>2</sub>

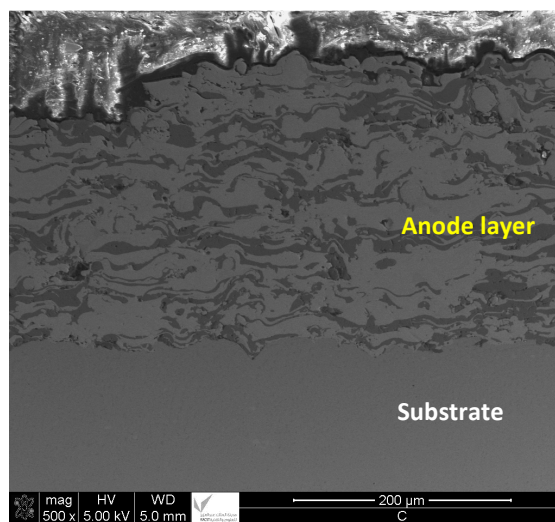
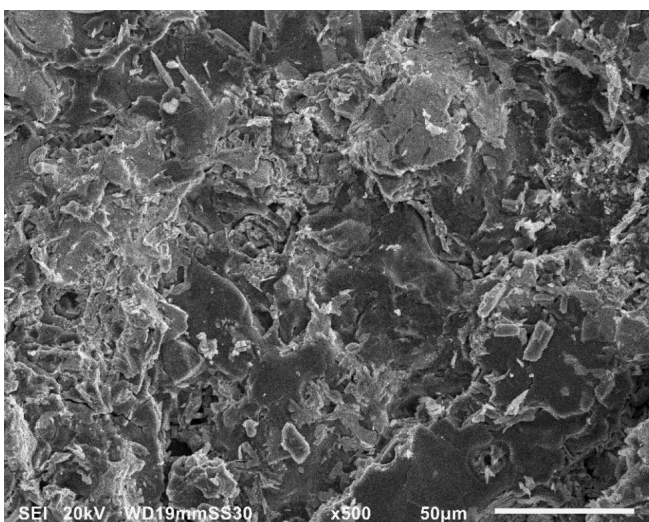


**Fig. 6.** SEM images of APS coated anode layer cross-section surfaces: (a) Mo-Mo<sub>2</sub>C/Al<sub>2</sub>O<sub>3</sub>, (b) Mo-Mo<sub>2</sub>C/ZrO<sub>2</sub> and (c) Mo-Mo<sub>2</sub>C/TiO<sub>2</sub>.

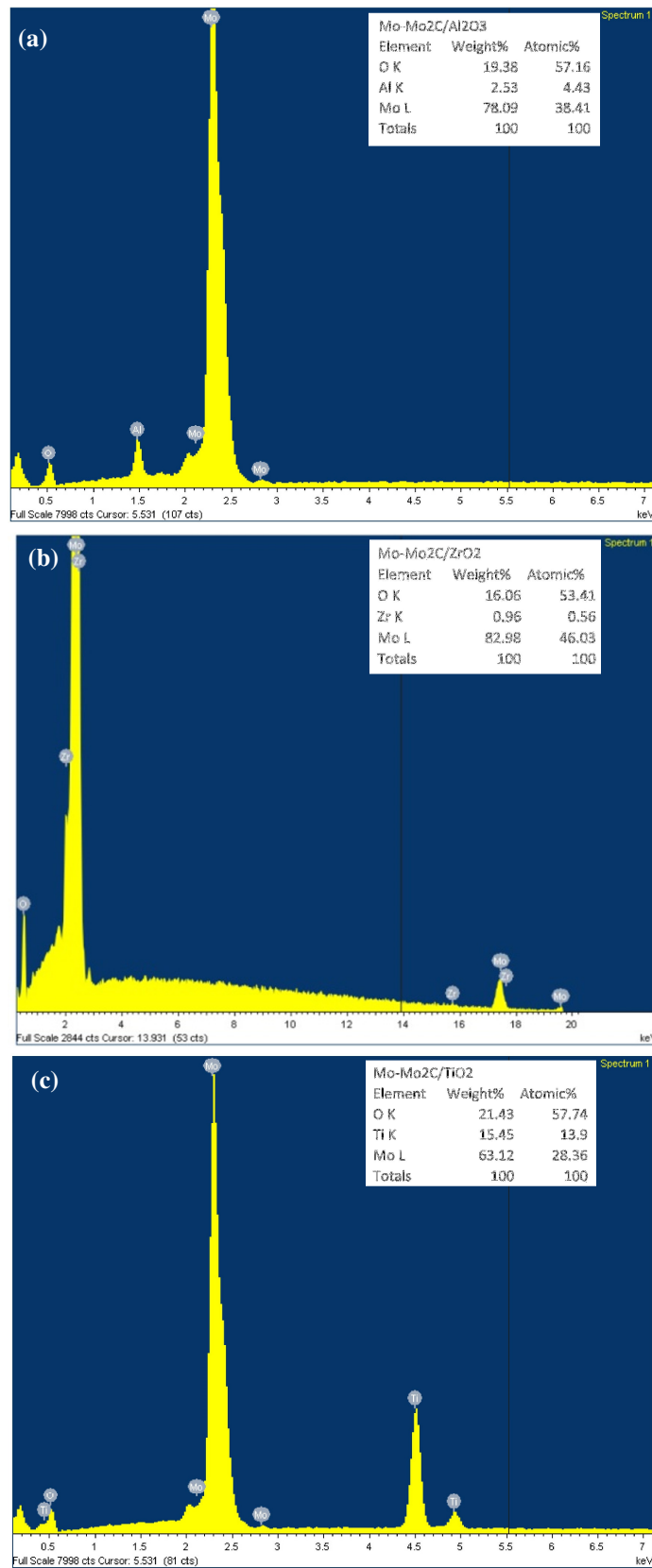


**Fig. 7.** EDX of APS coated anode layers: (a) Mo-Mo<sub>2</sub>C/Al<sub>2</sub>O<sub>3</sub>, (b) Mo-Mo<sub>2</sub>C/ZrO<sub>2</sub> and (c) Mo-Mo<sub>2</sub>C/TiO<sub>2</sub>.

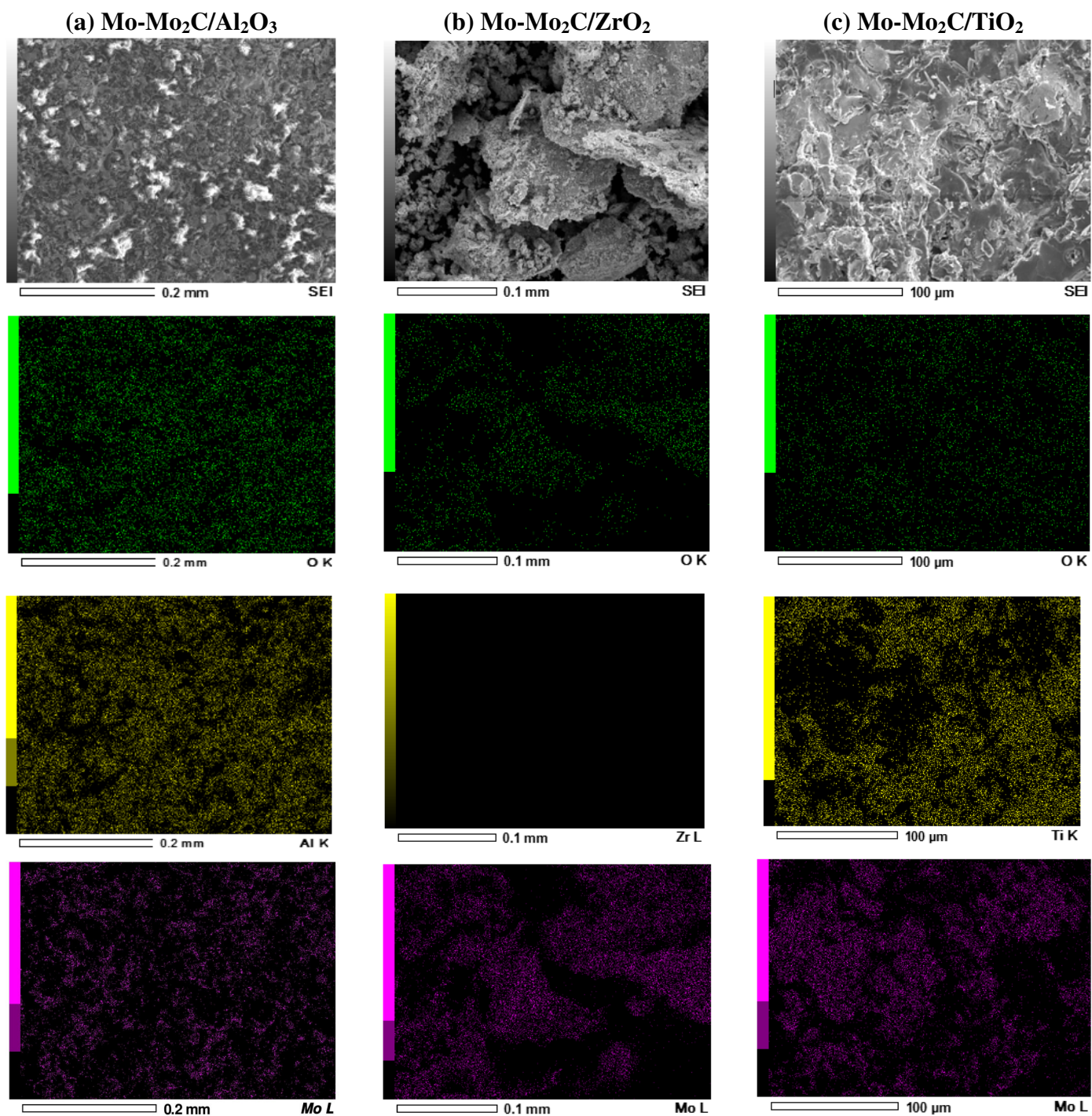


**Fig. 8.** EDX (elemental distribution or mapping) of APS coated anode materials: (a) Mo-Mo<sub>2</sub>C/Al<sub>2</sub>O<sub>3</sub>, (b) Mo-Mo<sub>2</sub>C/ZrO<sub>2</sub> and (c) Mo-Mo<sub>2</sub>C/TiO<sub>2</sub>.

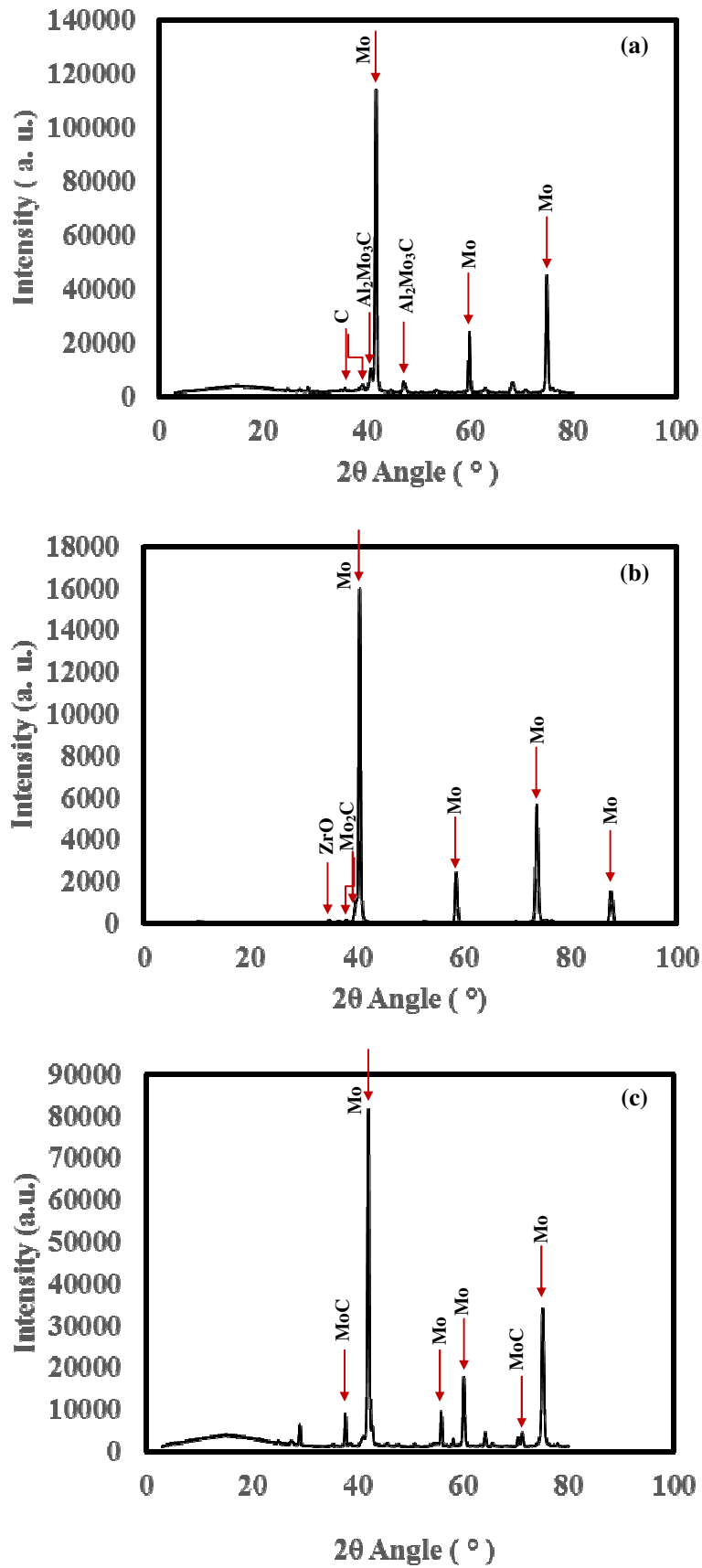


**Fig. 9.** XRD of APS coated anode layers (coating surface): (a) Mo-Mo<sub>2</sub>C/Al<sub>2</sub>O<sub>3</sub>, (b) Mo-Mo<sub>2</sub>C/ZrO<sub>2</sub> and (c) Mo-Mo<sub>2</sub>C/TiO<sub>2</sub>.

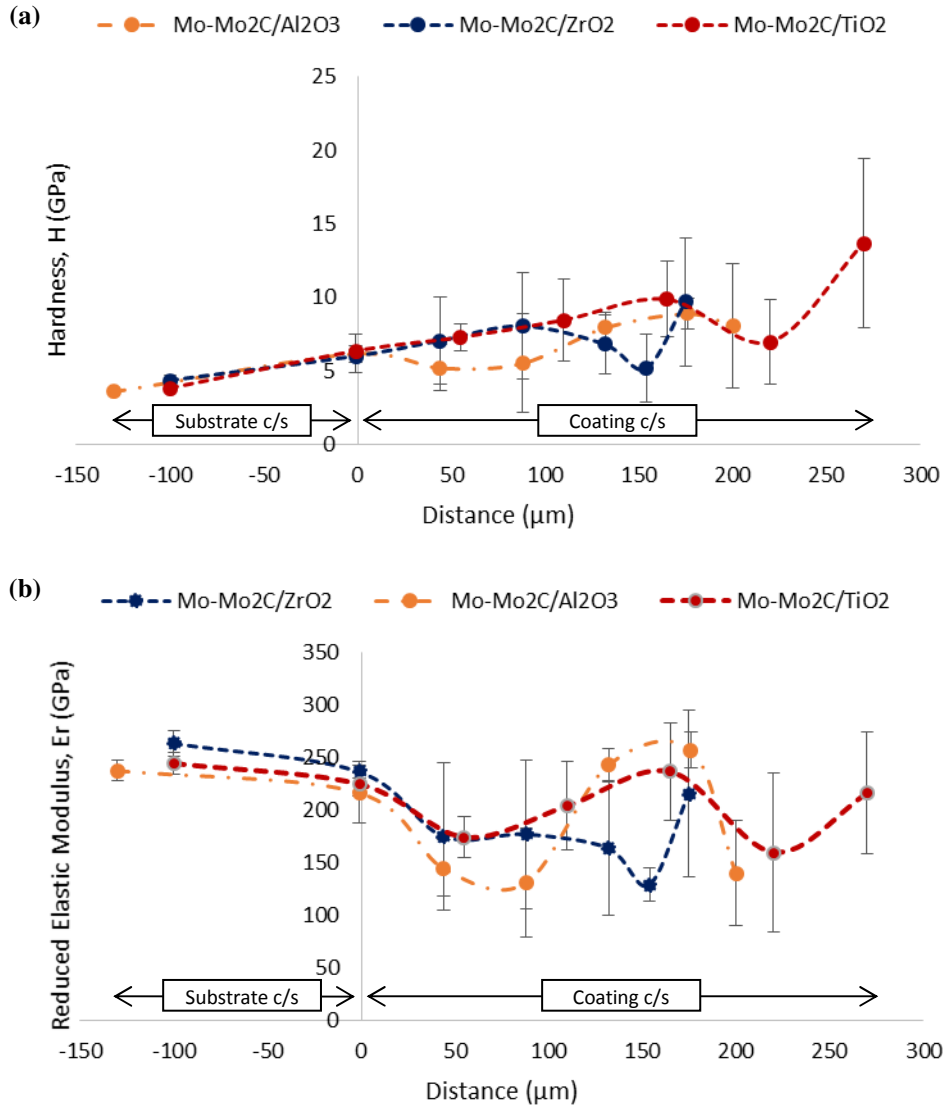


**Fig. 10.** Nanoindentation results (hardness and elastic modulus) of APS coated anode layer specimens (Mo-Mo<sub>2</sub>C/Al<sub>2</sub>O<sub>3</sub>, Mo-Mo<sub>2</sub>C/ZrO<sub>2</sub> and Mo-Mo<sub>2</sub>C/TiO<sub>2</sub>) on Hastelloy<sup>®</sup>X substrates.

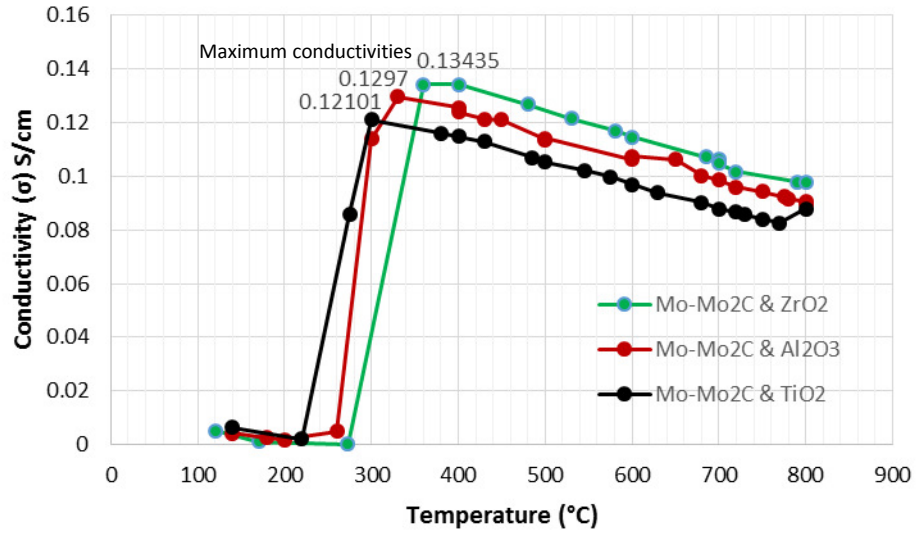


**Fig. 11.** Electrical conductivity variation with temperature: APS coated anode layer on Hastelloy<sup>®</sup>X substrate [Mo-Mo<sub>2</sub>C/Al<sub>2</sub>O<sub>3</sub>, Mo-Mo<sub>2</sub>C/ZrO<sub>2</sub> and Mo-Mo<sub>2</sub>C/TiO<sub>2</sub>].